J. Earth Syst. Sci. (2023)132 191
https://doi.org/10.1007/s12040-023-02206-x

Air-coast/inland footprints interaction in stable conditions during the AMMA SOP3 field experiment

Gislain R Mekompoamb[1,*], André Lenouo[2] and Clément Tchawoua[3]

[1] *Laboratory for Environmental Modelling and Atmospheric Physics, Department of Physics, Faculty of Science, University of Yaoundé 1, P.O. Box 812, Yaoundé, Cameroon.*
[2] *Department of Physics, Faculty of Science, University of Douala, P.O. Box 24157, Douala, Cameroon.*
[3] *Laboratory of Mechanics, Department of Physics, University of Yaoundé 1, P.O. Box 812, Yaoundé, Cameroon.*
Corresponding author. e-mail: mekompoamb2004@yahoo.fr

MS received 16 August 2022; revised 21 June 2023; accepted 13 August 2023

Radiosonde data recorded during the African Monsoon Multidisciplinary Analyses Special Observing Period 3 (AMMA SOP3) field campaign in West Africa (August 15–September 15, 2006) were used to examine air-coast/land coupling. Different turbulent radiosonde measurements were averaged over three levels (level 1: ~3 m, next level 2: ~10 m and lastly level 3: ~20 m) in the surface layer. These data enabled the comparison of turbulent fluxes with other variables, as well as the study of the scaling of surface layers for different areas in aerodynamically smooth/rough and relatively dry or wet conditions. Results showed stable and unstable stratifications at night-time. Drag coefficient over the coastal and inland footprints presents the same order of magnitude and could not be an indicator for the two different areas. However, the disparate night-time variation in sensible heat flux is substantially more pronounced over land than over the coast and can, therefore, be considered as an indicator of different surfaces. The underlying assumptions of Monin–Obukhov Similarity Theory (MOST) are consistently violated due to surface heterogeneities, but offsets from MOST are smaller for stable and unstable conditions, as well as for scaled standard deviations over the coast and overland. In addition, flux-profile relationships from MOST show a poor match with observations.

Keywords. AMMA field campaign; air–coast/inland interaction; Monin–Obukhov canonical functions; stable stratified boundary layer.

1. Introduction

The lower part of the troposphere in contact with the Earth's surface represents the atmospheric boundary layer (ABL). Being an essential and fundamental component of the Earth's climate, the investigation of the land surface–atmosphere exchange processes plays a prominent role in the ABL research including many related disciplines, e.g., weather forecasting, climate science, environmental impact studies, hydrology, and agricultural science. Quantifying air–land turbulent fluxes is of obvious relevance for modelling coupled atmosphere–land surface systems. Its study is critical for understanding pollution episodes because the pollutants emitted on the ground will be mixed and

Published online: 07 December 2023

diluted in the ABL. Also, a stably stratified boundary layer (SSBL) remains a matter of keen interest in fluid dynamics as the airflow generates a wide range of processes encompassing all scales of the atmospheric circulation.

Traditionally and within the limits of a homogeneous underlying surface, the MOST describes the surface fluxes (i.e., the flux-variance and flux-gradient) in the surface layer (Monin and Obukhov 1954), including thermal and aerodynamic roughnesses (Sorbjan 1989; Kaimal and Finnigan 1994; Wyngaard 2010). In addition, the sources of turbulent mixing as wind shear production and buoyancy production (Deardorff 1972; Moeng and Sullivan 1994) are variable in space and time; hence, accurate measurements and their parameterization are a challenge (Baklanov *et al.* 2011; Holtslag *et al.* 2013). Even as these assumptions are observable in many situations for one-dimensional processes, they remain violated on the coastal footprint where horizontal gradients are significant. The relatively dry inland footprints (compared to the coastal zone) are almost entirely aerodynamically rough with a low heat storage capacity, reflecting a low nightly cycle of sensible heat. The ocean surface is relatively smooth (compared to the Earth's) and has a very high heat storage capacity, making it able to store heat for a protracted period, thus fostering turbulent mixing at great depths with impacts on the diurnal cycle over the water. In contrast, the less watery (relatively drier) inland areas are rough and have low heat storage capacity, conveying a more pronounced diurnal cycle of sensible heat flux. Hence, the upland footprints are aerodynamically rough surfaces (higher sensible heat flux relative to the coast), whilst the coastal (water/land interface) surfaces are relatively smooth (aerodynamically) owed to their vicinity to the ocean.

The interaction sought is based on the transfer of turbulent coefficients in terms of heat and drag that affects the wind between the coast and the mainland, with its impact on the application of MOST.

Notwithstanding consistent literature outlining multitudes of experimental investigations of MOST for a horizontal and relatively homogeneous surface-atmosphere (Högström 1988; Stull 1988; Garratt 1992; Kaimal and Finnigan 1994; Grachev *et al.* 2005; Wyngaard 2010), very few studies are performed on coastal footprints and then compared to those on onshore. For the most part, observational studies in the coastal zone are primarily associated with measurements of turbulent transfer coefficients such as the drag coefficient, with a focus on deviations from MOST, the trend of the surface wave field over the water (Geernaert 1988; Mahrt and Geernaert 1999; Grachev *et al.* 2017). In addition, some investigations have also been carried out on the African continent (e.g., HAPEX-Sahel in 1992, DACCIWA in 2016), which have contributed to the development and applicability of MOST (Businger *et al.* 1971; Merry and Panofsky 1976; Nieuwstadt 1984; Mahrt *et al.* 1998). The HAPEX-Sahel (cf. Goutorbe *et al.* 1994) and DACCIWA (cf. Flamant *et al.* 2017) campaigns were conducted on a small scale (one or two sites), while the AMMA campaign was expanded (eight locations as part of this work). The complexity of the climatic and living conditions (famine, water scarcity, high temperature, deregulated rainfall cycle, the atmosphere–surface interaction (continental and oceanic)-climate) regulated by the West African monsoon (WAM), has allowed the scientific community to focus on this region of West Africa through the AMMA project. The lack of data in this region makes this project unique in terms of its scope and the means used (financial, human resources, and instrumentation). The AMMA project intensified in 2006, called Special Observing Periods (SOPs), is subdivided as follows: the pre-monsoon (SOP1), peak monsoon (SOP2), and the post-peak monsoon (SOP3) (Redelsperger *et al.* 2006).

During SOP3, air masses move from the sea to the land. These air masses, which interact with those of the continent, are at the source of several processes, especially MCS (Mesoscale Convective systems), LLJ (Low-Level Jet), advection (surface inhomogeneity), LLCs (low-level stratus clouds), gravity waves (Guichard *et al.* 2010). Penide *et al.* (2010) examined the processes (MCSs coupled with other variables) causing precipitation (not shown) in West Africa and revealed their strong presence and lifetime in this area during SOP3. Calm nights can suddenly become unstable due to their occurrence.

Variations in the structure of ABL, as well as local meteorological conditions near the surface, considerably affect the propagation of electromagnetic waves. Moreover, the usual meteorological characteristics and atmospheric refractivity are directly linked. Actually, the increase (or decrease) in atmospheric refractivity varies depending on whether a radio ray is bending upwards (or downwards). In a shallow layer near the surface with a negative refractive gradient still called a duct, any ray bending toward that surface can be 'trapped' (Brooks *et al.* 1999; Kaissassou *et al.* 2015, 2020, 2021; Grachev *et al.* 2017). As a result, electromagnetic waves can travel through the duct. The present contribution, performed within the framework of the AMMA program and specifically at SOP3 (August 15–September 15, 2006), aims to better understand ducting in the coastal and inland regions. This knowledge requires the controlled air-coastal/onshore exchanges, as well as the flow and turbulence properties in the ABL. The two classes of areas referred above are the coastal areas (Dakar, Douala, and Nouakchott) bordered by the Atlantic Ocean, and the onshore areas (Abuja, Agadez, Bamako, Niamey, and Tombouctou). This article is structured as follows: investigation area and data are outlined in the next section, numerical tools and methodology in section 3, results and discussion in section 4, and lastly, section 5 presents the conclusion.

2. Study area and data

The AMMA field program helped to generate the coastal and inland observational data, available in the AMMA database, collected through the Vaisala RS-80 and RS-92 sondes, which sampled every 2 s and provided data with vertical resolution ranging from 5 to 12 m, depending on the characteristics of each site and the meteorological conditions. Each sensor has a different relative humidity bias, which varies according to time of day and temperature. Indeed, Vaisala RS-80 models are known to have a high dry bias in humidity during the day and a lower one at night. Meanwhile, the Vaisala RS-92 models have a moderate dry bias during the day and low humidity at night. Given all these uncertainties about the moisture bias of radiosondes, assessment studies were performed using estimates of the integrated water vapour content derived from Global Positioning System (GPS) ground station measurements during the AMMA special observation period 2006. Correction functions (not shown) were applied to all sensor types (Vaisala RS-80, Vaisala RS-92) to correct for radiosonde bias, with the aim of significantly reducing vertical moisture and temperature measurement uncertainties (Karbou *et al.* 2012). According to Steinbrecht *et al.* (2008), Vaisala RS-80 radiosonde systems reveal lower temperatures in the daytime than Vaisala RS-92 systems. They also report some specifications for each type of radiosonde at 1000 hPa (surface layer). For RS-80, temperature (K) bias: $< \pm 0.2$, temperature accuracy: 0.3, pressure (hPa) bias: $< \pm 0.5$, pressure accuracy: 1.2. For RS-92, temperature (K) bias: $< \pm 0.2$, temperature accuracy: 0.15, pressure (hPa) bias: $< \pm 0.5$, pressure accuracy: 0.6. This allowed us to be in the surface layer depending on the three levels (level 1, about 3 m above the surface of each site, then level 2, $\sim$10 m and finally level 3, $\sim$20 m) chosen, and to better characterize and understand the ducting in this layer of the ABL. The AMMA SOP3 is peculiar in that it occurs after the turbulent period of the WAM, and so conditions from ABL to SOP3 (August 15–September 15, 2006) can be considered stable at night-time. Measurements at each site highlight the multi-scale spatial inhomogeneities of the ABL. The development of ABL over heterogeneous regions is of particular interest because of the non-stationary conditions, which conflict with the underlying hypotheses of MOST and consequently with the coupled environmental prediction and evaporation duct designs. Of the 20 or so active sites (as shown in figure 1) during the campaign, only eight were selected based on the low percentage of missing data and the type of data to be used in this work. The data collected are separated into two subgroups of surveys per day, at 12:00 UTC and 00:00 UTC, during the investigated period. Those of the subset of concern to us are those taken at 00:00 UTC, i.e., under stable conditions.

Mentes and Kaymaz (2007) examined the surface ducting conditions over Istanbul, Turkey, using radiosonde measurements recorded at the Göztepe meteorological station located on the Asian coast. Steiner and Smith (2002) and Mesnard and Sauvageot (2010) show the unsuitability of radiosonde data in the study of ducts due to their poor resolution (about 100 m). Meanwhile, Bech *et al.* (1998) in Barcelona report that the occurrence of surface ducts using low-resolution radiosonde data is 83% of those captured using high-resolution radiosonde measurements. Agusti *et al.* (2010) add that new equipment was deployed during the 2006 AMMA field season, enabling high vertical resolution (ranging from 5 to 12 m, between two successive levels) observations. All data collected during the AMMA

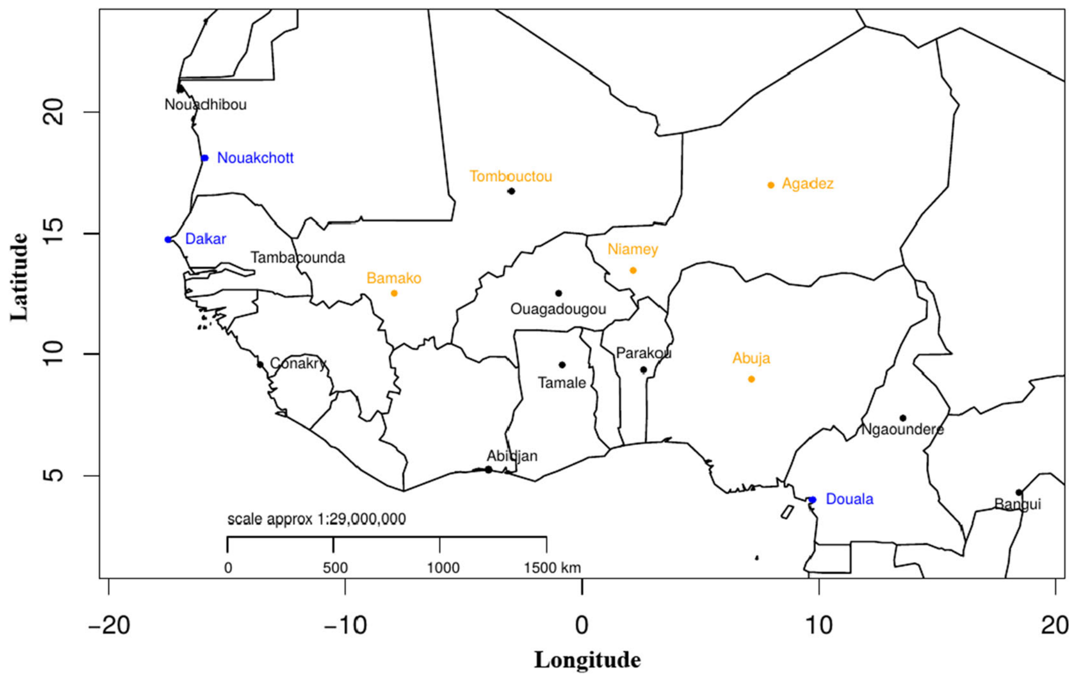

Figure 1. Summary map of AMMA's meteorological stations over West Africa, where horizontal axis represents longitude coordinates (from left (west) to right (east)), vertical axis is latitude coordinates (from down (south) to top (north)). The coloured locations (blue for coastal (Dakar, Douala, Nouakchott) and orange for onshore (Abuja, Agadez, Bamako, Niamey, Tombouctou)) represent those in our investigation.

Table 1. *Geographical coordinates and station altitudes in meters above sea level (m a.s.l.) including rates of nightly averaged data used per station during AMMA SOP3 campaign.*

Site	Location (Latitude–Longitude)	Altitude (m a.s.l.)	Number of data (percentage)
Coastal zone			
Dakar (Yoff)	14°44′N–17°30′W	28	20/32 (63%)
Douala	04°01′N–09°42′E	5	15/32 (47%)
Nouakchott	18°06′N–15°57′W	3	21/32 (66%)
Onshore zone			
Abuja	09°15′N–03°56′W	370	19/32 (59.5%)
Agadez	16°38′N–07°59′E	501	27/32 (84.5%)
Bamako	12°32′N–07°57′W	377	29/32 (91%)
Niamey	13°29′N–02°10′E	222	30/32 (94%)
Tombouctou	16°43′N–03°00′W	263	29/32 (91%)

campaigns have been recorded and stored in raw form and available in a common database (information online at http://database.amma-international.org). The radiosonde data are stocked in their original form, i.e., with a vertical resolution of an average 10 times more refined than a standard World Meteorological Organization (WMO) sounding (Faccani *et al.* 2009). The raw radiosonde data have a sampling rate of 2 seconds during the balloon ascent. As a result, radiosonde data are being used for this investigation. Table 1 summarizes the details of the data used for each location.

3. Numerical tools and methodology

Turbulent atmospheric data gathered during the 2006 AMMA SOP3 field campaign in West Africa are used to study the air-coast/inland coupling. Firstly, this work consists of outlining the daily averages of the nightly time series of some measured variables (wind speed and direction, air temperature, relative humidity) as well as other statistics (drag coefficient), including turbulent fluxes (sensible and latent heat) of the various sites, aiming to show the state of the meteorological conditions and the ruggedness of the surfaces, and the air-coastal/onshore footprints interaction. The drag coefficient is expressed as follows:

$$C_D = \left(\frac{u_*}{U}\right)^2 \tag{1}$$

where $u_* = (\langle u'w'\rangle^2 + \langle v'w'\rangle^2)^{1/4}$ (in m/s) and U (m/s) represent the friction and wind velocity, respectively. u', v' and w' are the wind turbulent fluctuations of longitudinal, lateral and vertical components of wind velocity.

The turbulent fluxes of latent heat H_L and sensible heat H_S can be written due to eddy-correlation method by:

$$H_L = L_e \rho \overline{w'q'} \tag{2}$$

and

$$H_S = c_p \rho \overline{w'\theta'} \tag{3}$$

L_e is the latent heat of evaporation of water, c_p is the specific heat capacity of air at constant pressure, q is the air-specific humidity, ρ is the mean air density, $\theta = T\left(\frac{1000}{P}\right)^{\gamma}$ is the potential temperature, with $\gamma = 0.286$, P is the pressure in hPa and T the temperature in Kelvin. The overbar represents an averaging operator.

Additionally, we compare and verify the validation of the universal Phi (Φ) functions whose empirical expressions were formulated by Kaimal and Finnigan (1994) in the 1968 Kansas field experiment, with the data collected from AMMA SOP3 under stable conditions (night-time) for the surface layer, over West Africa. The classical Φ functions from this landmark Kansas experiment were computed on flat, homogeneous surface footprints (Businger *et al.* 1971; Kaimal and Finnigan 1994). Thus, according to MOST, the non-dimensional vertical gradients of mean potential temperature (equation 4) and wind speed (equation 5), properly scaled, are universal functions of the Monin–Obukhov stability parameter (MOSP), scaled as follows:

$$\Phi_h(\zeta) = \left(\frac{\kappa z}{\theta_*}\right)\left(\frac{d\theta}{dz}\right) \tag{4}$$

and

$$\Phi_m(\zeta) = \left(\frac{\kappa z}{u_*}\right)\left(\frac{dU}{dz}\right) \tag{5}$$

with $\kappa = 0.4$ is the von Kármán constant, $\theta_* = -\overline{w'\theta'}/u_*$ is the scaling temperature.

Similarly, the normalized standard deviation of the velocity components σ_α (for $\alpha = u$ or $\alpha = v$), air temperature σ_θ and vertical velocity component σ_w are expressed as:

$$\Phi_\alpha(\zeta) = \frac{\sigma_\alpha}{u_*} \tag{6}$$

$$\Phi_\theta(\zeta) = \frac{\sigma_\theta}{|\theta_*|} \tag{7}$$

$$\Phi_w = \frac{\sigma_w}{u_*} \tag{8}$$

where $\zeta = z/L$ is the MOSP (z is level and $L = -(\theta_{00} u_*^2/\kappa g \theta_*)$ is the Obukhov length). θ_{00} here is the reference temperature near the ground.

The coupling between the different computations and the necessary settings made on each zone enables us to discuss this in the next section.

4. Results and discussions

4.1 *Measured atmospheric turbulence parameters*

The aim of the traditional time series is to present an overview of the distribution and sampling of relevant variables, the meteorological conditions of the region, and additional information not usually derived from the scattered plots. Figure 2 outlines the time series of wind speed and direction, air temperature, and relative humidity, averaged daily at each coastal site and over three levels, as shown in table 2. The time distributions of wind speed (all typically <6 m/s) and direction over the coastal footprints are nearly similar, with wind speeds over Douala near neutral. Douala also has cooler temperatures than Dakar and Nouakchott. Douala's surface humidity decreases from level 1 to level 3, Dakar's is deeper in level 3 than in the others, while in Nouakchott, the gaps are negligible. In figure 3, the Tombouctou site shows higher wind speed intensities on all three levels and low for the Abuja and Bamako stations. The wind speeds at the onshore parcels are almost similar to those at the

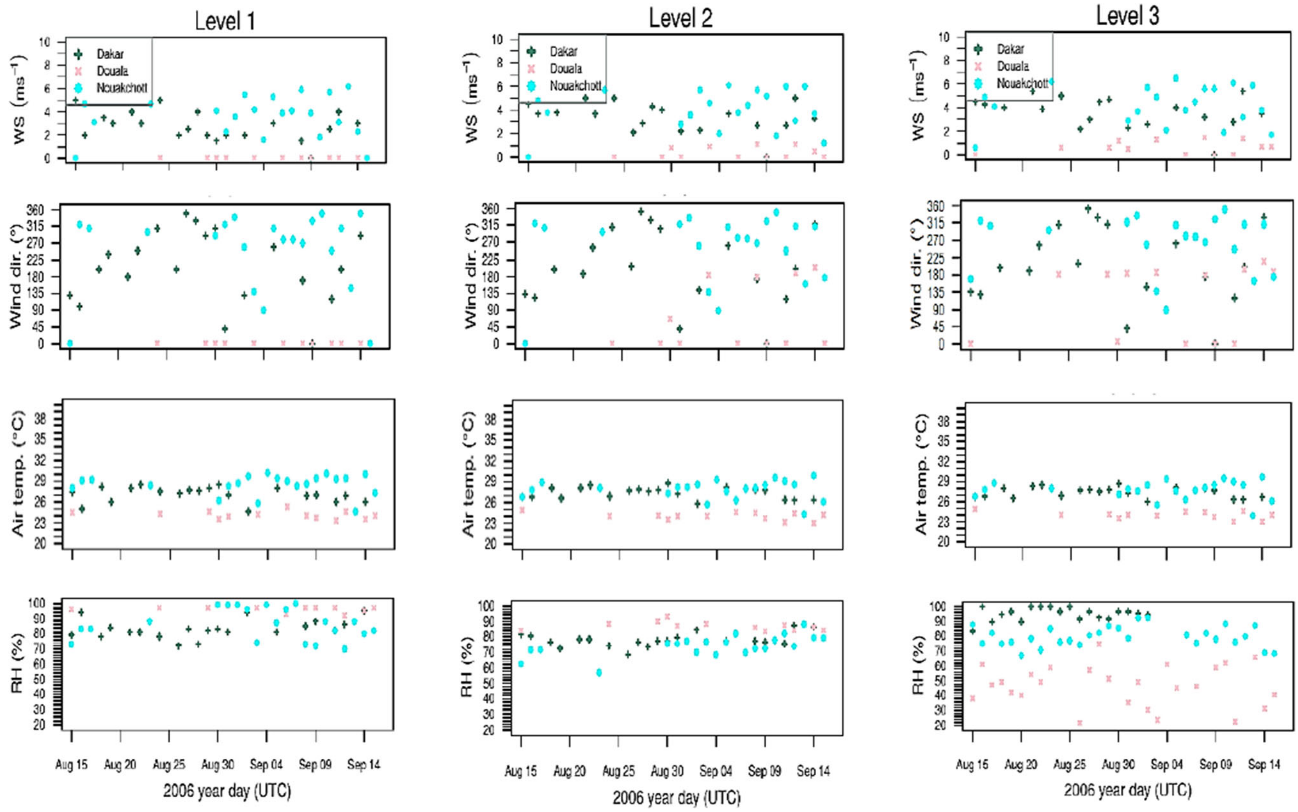

Figure 2. Time series of nightly averages (00.00 UTC) of wind speed (1st row), wind direction (2nd row), air temperature (3rd row), and relative humidity (4th row) over the three levels (see table 2) for the coastal footprints (Dakar, Douala, Nouakchott) from August 15 to September 15, 2006.

Table 2. *Instrumentation, parameters and averaged measurement height in meters above ground level (m a.g.l.) for each site during AMMA SOP3 campaign.*

Site	Type of Vaisala radiosonde	Parameter	Measurement height (in m a.g.l.)
Dakar (Yoff)	RS-80; RS-92	Wind speed (WS), wind direction (DD), air temperature (T), relative humidity (RH), air-pressure (P), dew point (Td), altitude (z)	2; 7.85; 17.75 (levels 1–3)
Douala	RS-80; RS-92	WS, DD, T, RH, P, Td, z	2; 15; 25.54 (levels 1–3)
Nouakchott	RS-80; RS-92	WS, DD, T, RH, P, Td, z	5; 14.71; 21.05 (levels 1–3)
Abuja	RS-92	WS, DD, T, RH, P, Td, z	2; 10.42; 21.47 (levels 1–3)
Agadez	RS-80; RS-92	WS, DD, T, RH, P, Td, z	2; 10.37; 21.52 (levels 1–3)
Bamako	RS-80; RS-92	WS, DD, T, RH, P, Td, z	5; 19.65; 28.69 (levels 1–3)
Niamey	RS-80; RS-92	WS, DD, T, RH, P, Td, z	5; 14.67; 27.23 (levels 1–3)
Tombouctou	RS-80; RS-92	WS, DD, T, RH, P, Td, z	5; 34.13; 42.10 (levels 1–3)

coastal sites. The nocturnal time series of wind directions are patchy and typically range from 90° to 315°. Tombouctou and Agadez are warmer, with air temperatures around 30°C, while Abuja is colder (air temperature $<$ 25°C). The air is more humid in Abuja and Bamako, but more pronounced in Abuja, reaching practically 100% on all three levels. This contrasts with the air in Tombouctou and Agadez, which is drier (RH $<$ 75%), justifying their status as Sahelian cities. Based on the comparison of the two categories of sites in a global way, the studied parameters (wind speed, wind direction, air temperature and relative humidity) are quasi-similar in both types, in spite of some specificities.

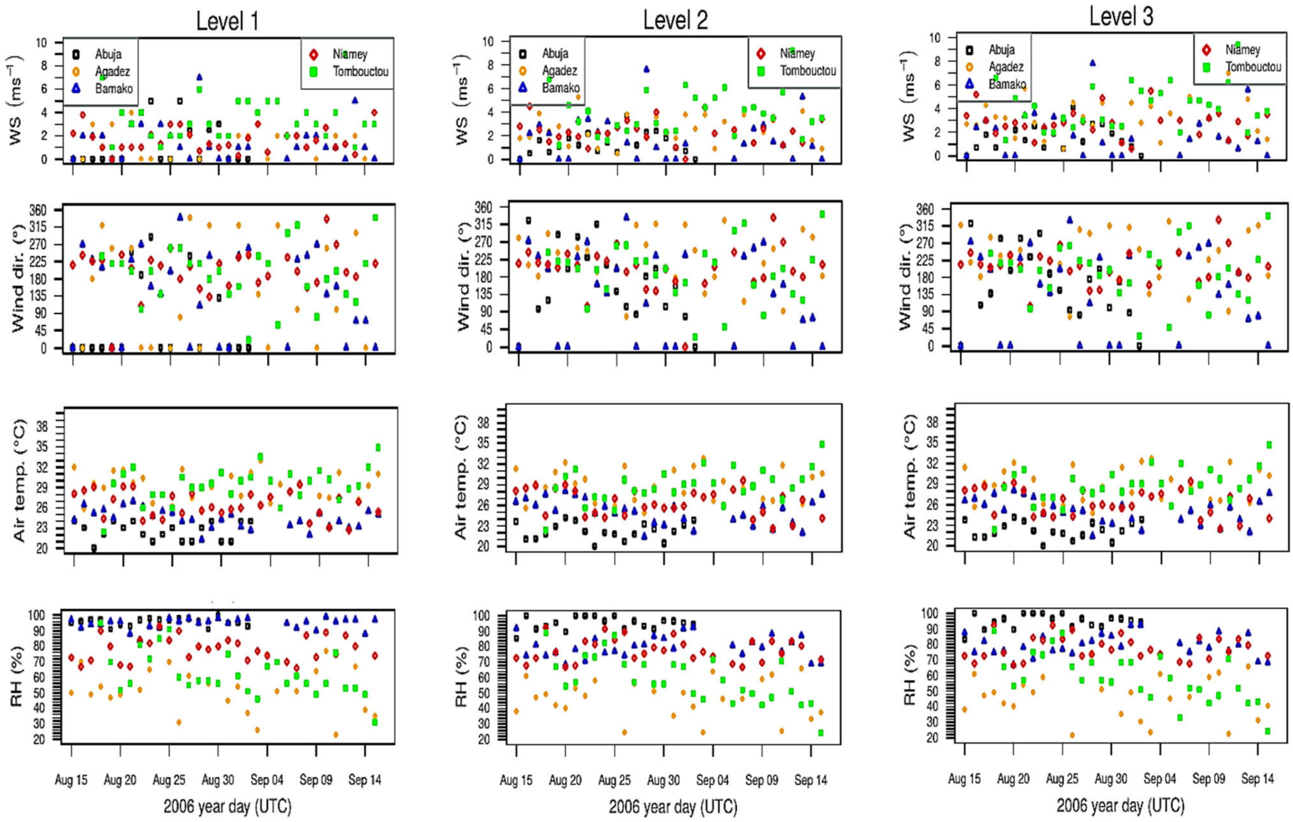

Figure 3. Time series of nightly averages (00.00 UTC) of wind speed (1st row), wind direction (2nd row), air temperature (3rd row), and relative humidity (4th row) over the three levels (see table 2) for the mainland footprints (Abuja, Agadez, Bamako, Niamey, Tombouctou) from August 15 to September 15, 2006.

4.2 *Turbulent fluxes and the MOSP*

The magnitude of the averaged night-time values of friction velocity is approximately similar on both coastal and inland surfaces (see figure 4). Douala (figure 4a, b, c) outlines a relatively smoother surface than all the others; in contrast, Nouakchott and Tombouctou have the roughest surfaces. Friction velocity is thus disparately distributed and can therefore, fluctuate greatly (increasing or decreasing) from one night to the next. In view of these findings, friction velocity is not an accurate indicator to typify the two types of surfaces (coastal and inland).

Figure 5 explores the nightly averages of the drag coefficient plotted versus wind direction. This figure reveals a wind speed slope ranging from 100 to about 350° at coastal sites, while this slope ranges from 45 to 340° at inland areas. Despite the low values of the drag coefficient observed at the coastal sites of Dakar and Nouakchott, its amplitude remains close to that of the inland areas. The non-existence of C_D values (figure 5a) for level 1 at the Douala site reflects the neutrality of the wind's velocity. The order of magnitude of C_D over the investigated areas is $C_D = 1.10^{-1}$, with the majority of the values below 0.4. This order contrasts with $C_D \approx 1.10^{-3}$ obtained by Grachev *et al.* (2017) over the North Carolina coastal area during the CASPER-East field experiment between October and November 2015, conveying relatively smoother surfaces. The influence of obstacles on the different sites, in general, is very inconspicuous. The turbulent air shear flow in the African coastal areas becomes as complex as that in the inland. Because of the discontinuity (inhomogeneity) of the coastal footprint and a similar order of magnitude, the drag coefficient cannot be an indicator between coastal and inland sites in West Africa.

Figures 6 and 7 highlight the time series of turbulent fluxes (H_S and H_L) at each site. Traditionally, the sign convention specifies stable stratifications when $H_S < 0$ and unstable for $H_S > 0$. In view of these features, we depict stable and unstable stratifications on the coast and inland (figures 6 and 7). Note also that the magnitudes of H_S are larger inland than on the coast, values linked to the different specific heat

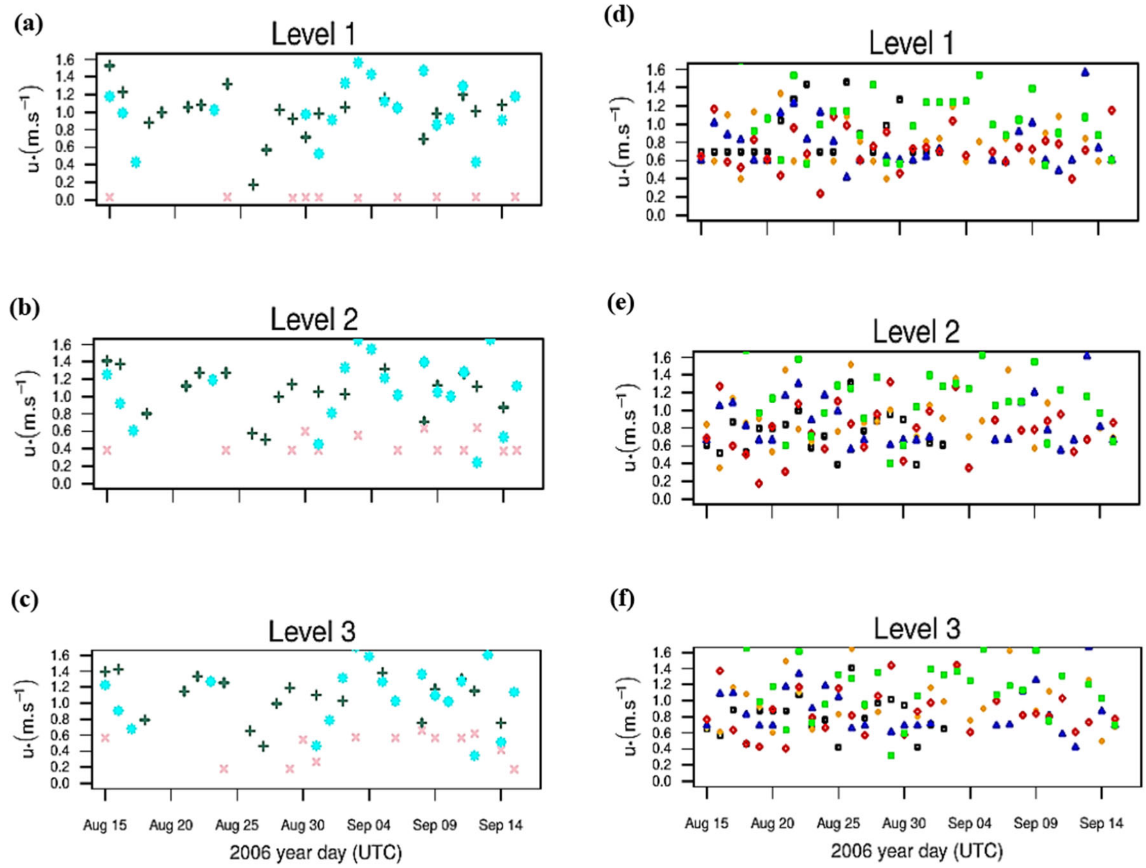

Figure 4. Time series of nightly averages (00.00 UTC) of friction velocity u_* over the three levels (see table 2) for the coastal footprints **(a, b, c)** and mainland footprints **(d, e, f)** from August 15 to September 15, 2006. The symbols are the same as those in figures 2 (for coastal areas) and 3 (for mainland areas).

capacities and aerodynamic properties of the underlying surfaces. In contrast, the amplitude of H_L (figure 7) is virtually identical both on the coast and inland, reflecting the similarity of the two types of underlying surfaces in terms of latent heat flux. Additionally, figure 8 reports the temporal patterns of MOSP ($\zeta = z/L$); this figure shows the type, number, and degree (weak or strong) of stratification periods observed. According to the sign convention, $\zeta > 0$ indicates a stable stratification or a stable boundary layer (SBL) and unstable or a convective boundary layer (CBL), when $\zeta < 0$. The amplitude of ζ is substantially more pronounced inland than on coastal surfaces, and its values in the surface layer as one moves away from the surface, i.e., the level. Except for the Douala location, the values at all coastal sites (at all levels), as well as those at level 1 of all inland sites, tend towards neutrality, i.e., $\zeta \rightarrow 0$ (see figure 8a, b, c, d). These values are more prominent at levels 2 and 3 of the inland surfaces (figure 8e, f).

In the down part of the ABL (surface layer), the MOST describes the average temperature of a fluid in the layer, the aerodynamic and thermal roughnesses, and the flow as a function of height, under the conditions of a stable non-neutral atmosphere. Because of the jaggedness of the various surfaces, the results generated (e.g., the variance of the various fluxes) sparsely point to a neutral atmosphere, hence the violation of MOST.

The description and interpretation of the notion of atmospheric turbulence rely strongly on the upwind 'flux markers' on which the different statistics have been sampled. Typically, flux markers are locations that lie at some distance along with the upwind fetch and actually contribute to the initiation and sinks of a signal (Leclerc and Foken 2014). Kljun *et al.* (2004), Klaassen and Sogachev (2006), and Glazunov *et al.* (2016) indicate that existing marker models attempt to describe the position and extent of the surface contributing to the sampling of a turbulent flux as a function of windward distances, thermal stratification, ground roughness, and measurement height. Thus, for heterogeneous surfaces such as those in our study, measurements collected at

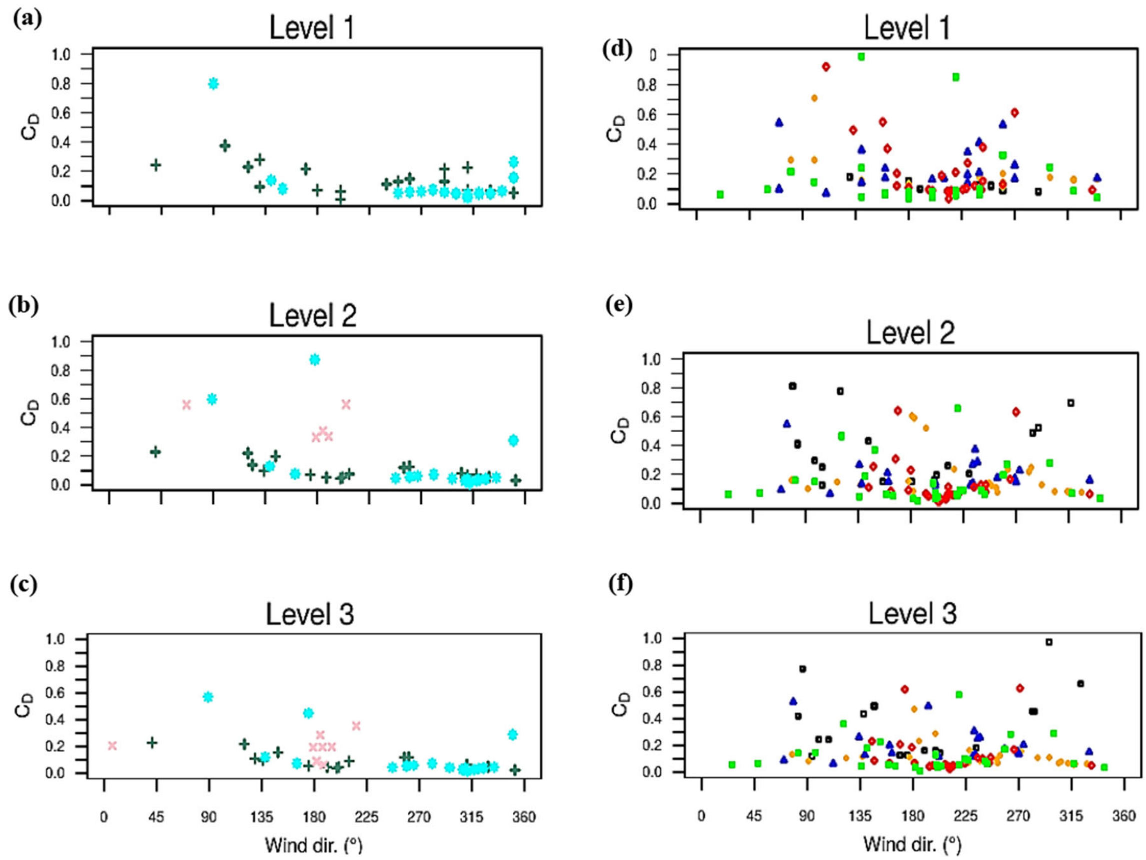

Figure 5. Nightly averages of the drag coefficient plotted versus wind direction for data recorded during the AMMA SOP3 field campaign (August 15–September 15, 2006) on the three levels (see table 2), for the coastal **(a, b, c)** and mainland **(d, e, f)** areas. The symbols are the same as those in figures 2 (for coastal areas) and 3 (for mainland areas).

different levels may have very different flux markers that correspond to either an aerodynamically rough or relatively smooth surface. This steep change in surface characteristics due to the coast-inland transition causes the development of an internal boundary layer (IBL). So, according to the observations of the measurements sampled during the AMMA SOP3 campaign, the sensible heat flux could be qualified as an indicator of the different surface footprints.

4.3 *Applicability of MOST in the inland and coastal zones*

The dataset collected during the AMMA SOP3 campaign permits us, in this section, to examine the classical MOST universal functions over heterogeneous terrain by comparing them to those established during the Kansas 1968 field campaign over uniform flat surfaces.

All correctly scaled turbulence statistics, especially the dimensionless vertical gradients of potential temperature (equation 4) and mean wind speed (equation 5), are universal MOSP functions (ζ). Similarly, the normalized standard deviations of the wind speed and air temperature components are defined by equations (6 and 7), respectively. Although traditionally, field experiments establish the exact forms of universal functions, there is nevertheless asymptotic modelling in the prediction of these functions for the cases of strong stable stratification ($\zeta > 1$) and extreme instability ($\zeta < -1$), through self-similarity assumptions (Stull 1988; Kaimal and Finnigan 1994; Wyngaard 2010). Studying similarity functions (equations 4–7) requires filtering the data to extract spurious ones, as described by Grachev *et al.* (2016). Figure 9 exposes the plot of the normalized standard deviation of the vertical velocity component Φ_w as a function of the local MOSP (ζ) of the collected turbulent data. These data were sectioned into stable ($\zeta > 0$, figure 9a, b) and unstable ($\zeta < 0$, figure 9c, d) conditions to evaluate the MOSP at different levels of the local scale. Other similar graphs of the normalized standard deviation of the longitudinal velocity component Φ_u versus ζ are shown in figure 10. From figures 9 and 10, the two

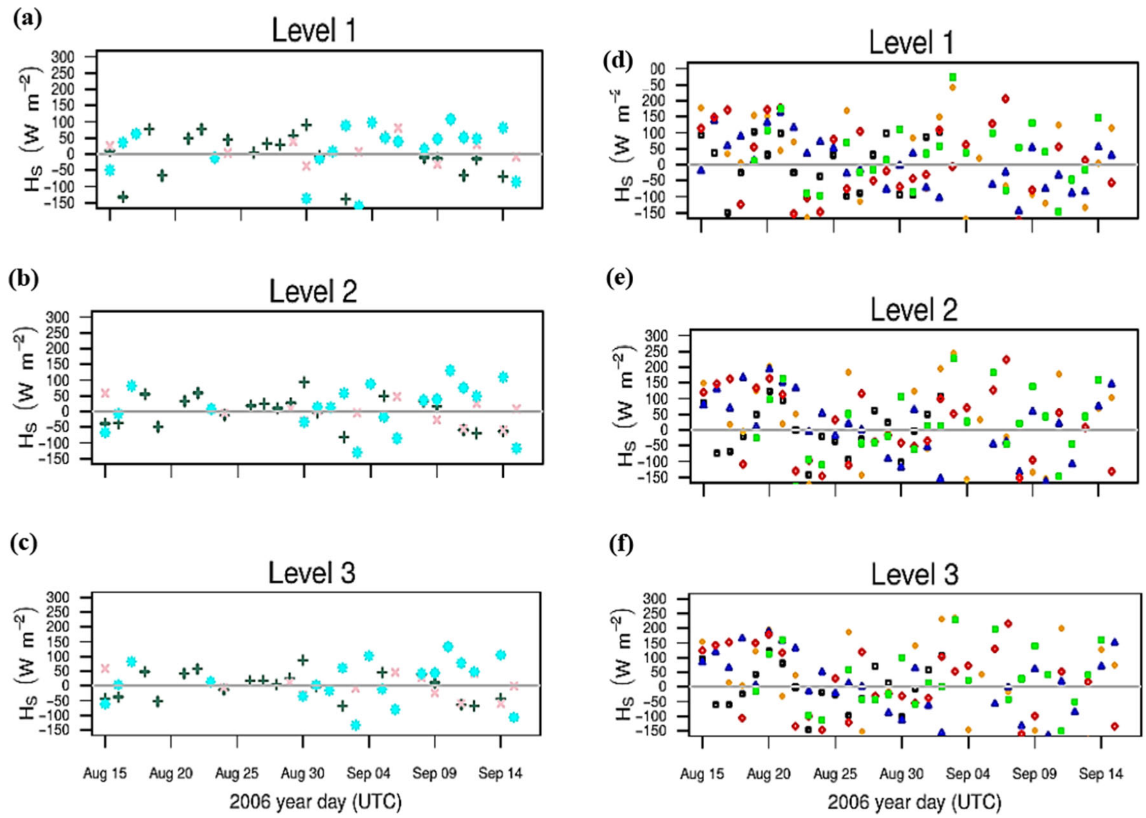

Figure 6. Time series of nightly averages (00.00 UTC) of sensible heat flux H_S over the three levels (see table 2) for the coastal footprints **(a, b, c)** and mainland footprints **(d, e, f)** from August 15 to September 15, 2006. The horizontal gray line indicates the boundary between a stable boundary layer ($H_S < 0$) and a convective boundary layer ($H_S > 0$). The symbols are the same as those in figures 2 (for coastal areas) and 3 (for mainland areas).

universal functions $\Phi_u(\zeta)$ and $\Phi_w(\zeta)$ are consistent with the local-scale MOST predictions. Moreover, the averaged data from the different levels converge reasonably well to a unique universal curve; in particular, $\Phi_w(\zeta)$ and $\Phi_u(\zeta)$ are approximately uniform for $\zeta > 0$. Grachev *et al.* (2017) prove that the same results are obtained for the normalized standard deviation of the lateral component of the velocity $\Phi_v = \sigma_v/u_*$, not shown (with $\Phi_v \approx 1.80$ when $|\zeta| \to 0$). As expected in the near-neutral regime, the asymptotic boundaries predict that $\Phi_u(0) > \Phi_v(0) > \Phi_w(0)$, underscoring the anisotropy of the airflow. Our results agree with the classical results produced by Panofsky and Dutton (1984), who argue that $\Phi_w(0) = 1.25$, $\Phi_v(0) = 1.91$ and $\Phi_u(0) = 2.39$, which are derived from data gathered from the flat surface overland under near-neutral stability conditions.

Figure 11 shows the plot of the dimensionless standard deviation of potential temperature versus ζ. Grachev *et al.* (2003, 2008) show the ambiguity of Φ_θ for near-neutral conditions because when ζ tends to zero, the temperature scale θ_* also tends to zero asymptotically. They add that under these near-neutral conditions, σ_θ has finite values associated with thermally heterogeneous surfaces. Regardless of the behaviours of these different quantities, we nevertheless find that the averaged data asymptotically follow the classical MOST curves (figure 11) except for the highly stable and near-neutral cases; indeed, Φ_θ is approximately constant for $\zeta > 0$ (figure 11a, b), but decreasing ζ leads to decreasing Φ_θ when $\zeta < 0$ (figure 11c, d). Furthermore, the bulk of our computed Φ_θ values consistently lie above the plotted curves for our two classes of surfaces.

So far, the results of the evaluation of normalized standard deviations of vertical velocity (Φ_w), longitudinal velocity (Φ_u) and temperature (Φ_θ) for our different surfaces using the data collected (nightly averaged) during the AMMA SOP3 campaign at multi-level in the surface layer (about 10%) of the ABL, qualitatively and closely corroborate with those from the flat and homogeneous areas where MOST is applied. Our results are found in the limit of low stability, i.e., $0 < \zeta < 1$, and low convection

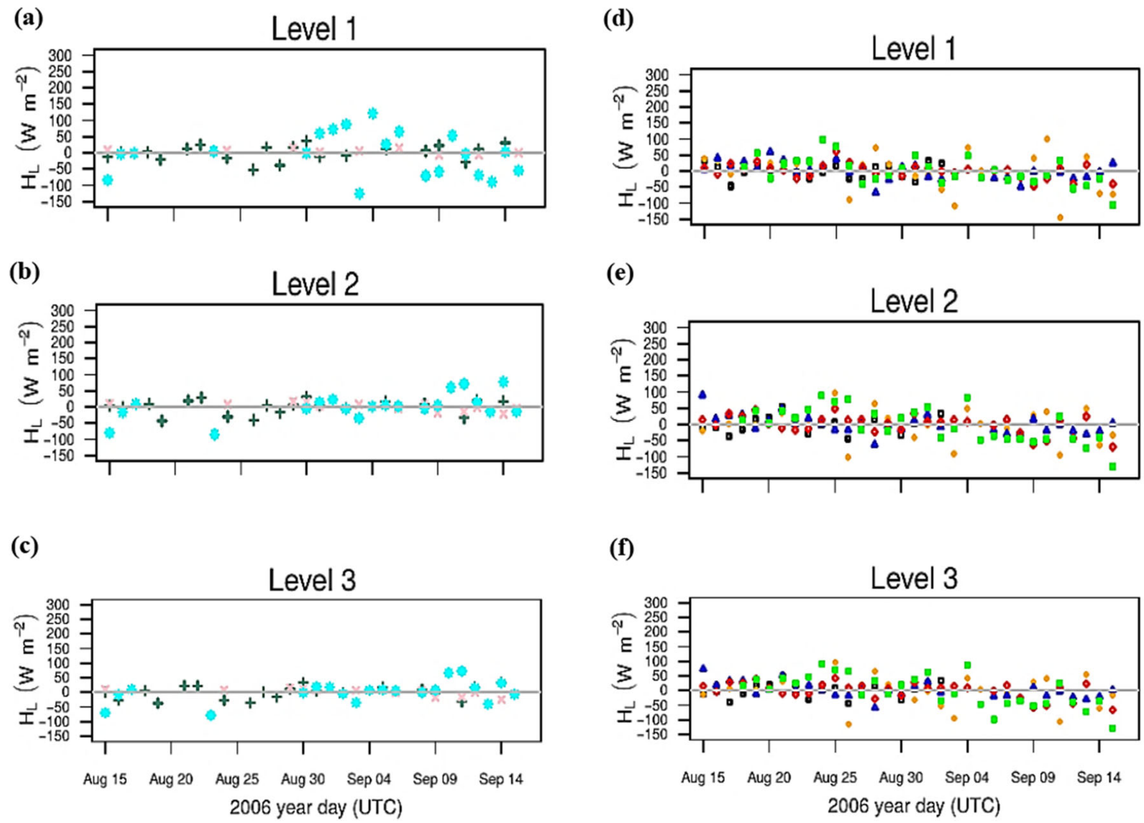

Figure 7. Time series of nightly averages (00.00 UTC) of latent heat flux H_L over the three levels (see table 2) for the coastal footprints **(a, b, c)** and mainland footprints **(d, e, f)** from August 15 to September 15, 2006 of AMMA campaign. The symbols are the same as those in figures 2 (for coastal areas) and 3 (for mainland areas).

(instability), i.e., $-1<\zeta<0$, on all surfaces of the eight locations studied in West Africa.

Equations (4 and 5) define the multi-level flux-profile relationships, or simply the link between the dimensionless vertical gradients of potential temperature (Φ_h) and mean wind speed (Φ_m) with the turbulent fluxes. Φ_h and Φ_m are estimated in a layer that is several meters deep. Indeed, their evaluation is based on the finite difference method such that to estimate the vertical gradients at an intermediate level x, linear interpolations of the potential temperature and wind speed from the adjacent levels $x-1$ and $x+1$ are performed.

The dimensionless vertical gradient of mean wind speed Φ_m is plotted as a function of ζ and then plotted in figure 12 according to equation (5) for both stable and unstable conditions. It can be seen in figure 12 that the averaged data disagree with the canonical Businger–Dyer expression in the convective case (see figure 12c, d); this observation contrasts with that made in the stable case where the data appear to agree poorly with the classical expression (figure 12a, b). Similarly, analogous plots are made for the dimensionless vertical gradient of the mean potential temperature Φ_h versus ζ according to equation (4) and shown in figure 13. The scatter in the averaged data does not support the classical Businger–Dyer formulations. Thus, the flux-profile and more precisely flux-gradient similarity relations of Φ_m and Φ_h are not consistent. Exploiting eddy covariance data collected over a pine forest, and data obtained over an alpine slope, Rannik (1998) and Nadeau *et al.* (2013) respectively concluded that flux-gradient similarity performs worse than flux-variance similarity.

The reason for the inconsistency of MOST in the plots of Φ_m and Φ_h versus ζ (figures 12, 13) is due to self-correlation. Indeed, the identical variables (e.g., the friction velocity u_*) are involved in both the definition of MOSP and the universal functions, reflecting a weak trend in the data. However, this self-correlation problem can be adjusted by creating and plotting, for example, a 'mixed' universal function or a stability parameter by removing u_*. This mixing becomes the combination (multiplication) of any universal function with the inverse of another function such that we have

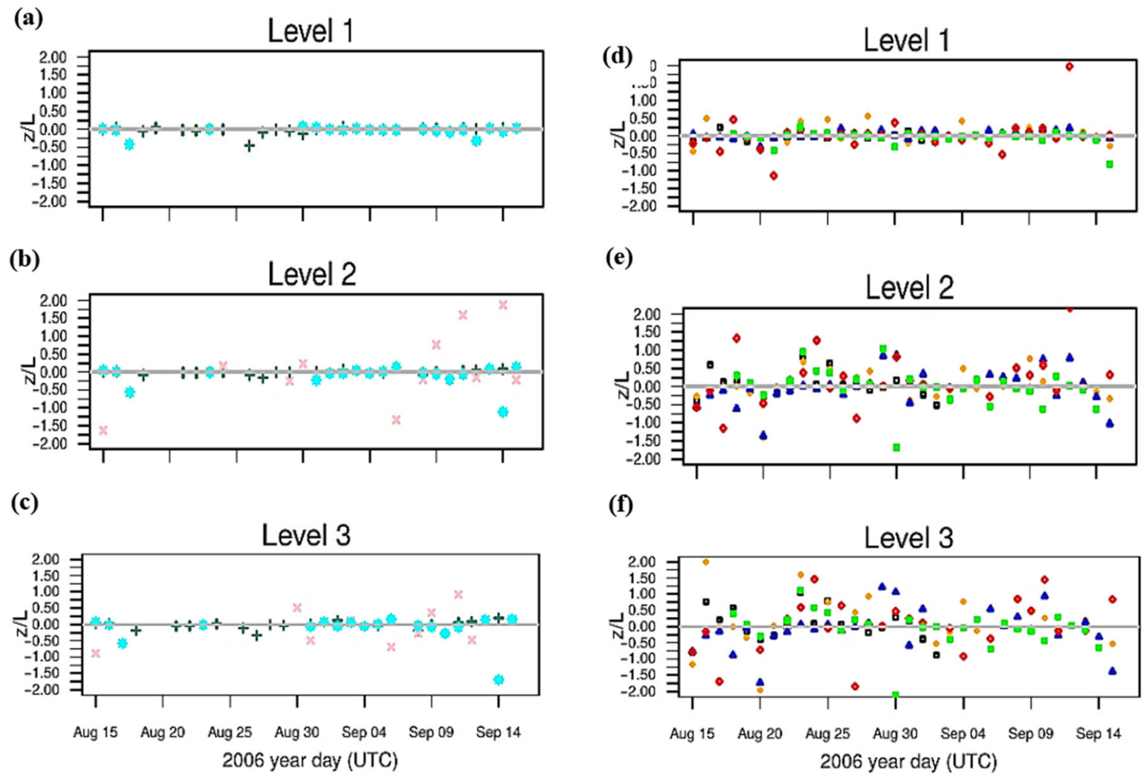

Figure 8. Time series of nightly averages (00.00 UTC) of MOSP $\zeta = z/L$ on the three levels (see table 2) for the coastal footprints **(a, b, c)** and mainland footprints **(d, e, f)** from August 15 to September 15, 2006. The horizontal gray line indicates the boundary between a stable boundary layer ($\zeta > 0$) and a convective boundary layer ($\zeta < 0$). The symbols are the same as those in figures 2 (for coastal areas) and 3 (for inland areas).

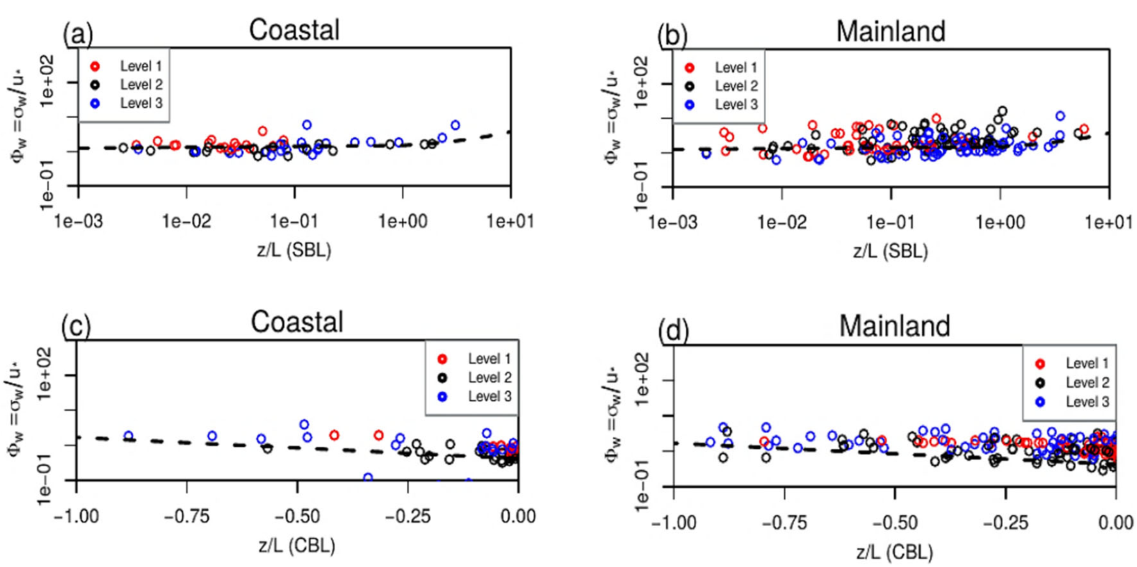

Figure 9. Plots of the non-dimensional standard deviation of the vertical velocity component (Φ_w) versus local MOSP (ζ) for the nightly averages data recorded during the AMMA SOP3 field campaign (August 15–September 15, 2006) over the coastal **(a, c)** and mainland **(b, d)** footprints. Figures (a) and (b) correspond to stable conditions ($\zeta > 0$), or the stable boundary layer (SBL); figures (c) and (d) reflect the unstable conditions ($\zeta < 0$), or the convective boundary layer (CBL). The dashed lines represent the $\Phi_w = 1.25(1 + 0.2\zeta)$ for $\zeta > 0$ and $\Phi_w = 1.25(1 - 3\zeta)^{1/3}$ for $\zeta < 0$.

terms $\Phi_m\Phi_u^{-1}$, $\Phi_h\Phi_w^{-1}$, $\Phi_u\Phi_w^{-1}$, and so on. Self-correlation does not affect these new hybrid functions because apart from the height z, they do not share any variables with ζ. To prune this sensitivity from the self-correlation dependence, we define the following function:

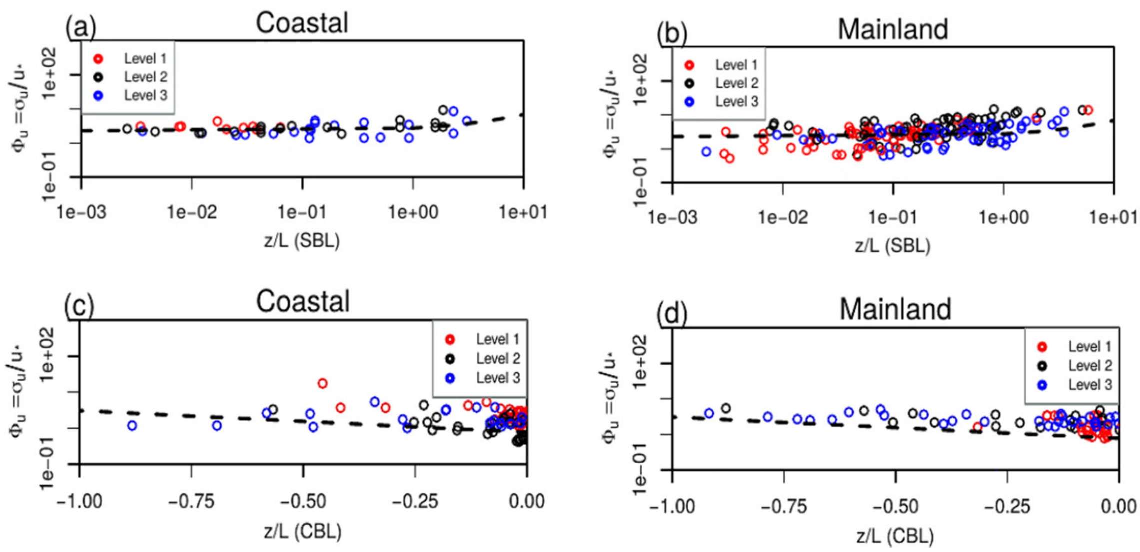

Figure 10. As for figure 9, but for the normalized standard deviation of the longitudinal velocity component (Φ_u). The dashed lines correspond to $\Phi_u = 2.3(1 + 0.2\zeta)$ for $\zeta > 0$ **(a, b)** and $\Phi_u = 2.3(1 - 3\zeta)^{1/3}$ for $\zeta < 0$ **(c, d)**.

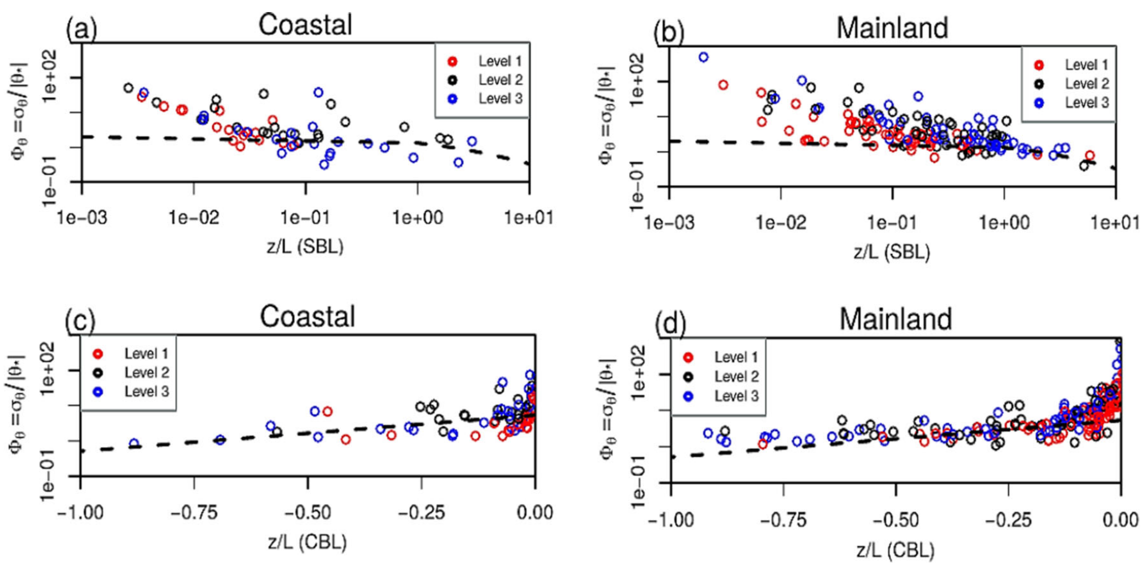

Figure 11. As for figure 9, but for the normalized standard deviation of the temperature (Φ_θ). The dashed lines correspond to $\Phi_\theta = 2(1 + 0.5\zeta)^{-1}$ for $\zeta > 0$ **(a, b)** and $\Phi_\theta = 2(1 - 9.5\zeta)^{-1/3}$ for $\zeta < 0$ **(c, d)**.

$$\Phi_m \Phi_w^{-1} = \left(\frac{\kappa z}{\sigma_w}\right) \frac{dU}{dz}. \quad (9)$$

This universal function of equation (9) yields the plot in figure 14. Figure 14 shows a dispersion of data that does not change significantly around the curves from the canonical formulations developed in Kansas, so that autocorrelation does not affect our results overall.

Since universal functions are a means of assessing local degrees of dispersion as well as general trends (figures 9–14), the bin-averaged data can produce additional information for us. Figures 15, 16, and 17 display the bin-averaged relationships of the non-dimensional functions Φ_m, Φ_h, and Φ_w evaluated at different levels as a function of ζ using data gathered for both stable and unstable conditions, and separately for coastal (Dakar and Nouakchott) and inland (Bamako and Niamey) flows. The two examples chosen per category (coastal and onshore) are based on the density of data collected, as presented in table 1.

By exploiting the bin-averaged values of Φ_w observed at different levels during the coastal and inland flows in figure 15, we find that they collapse quite well to a single universal curve while

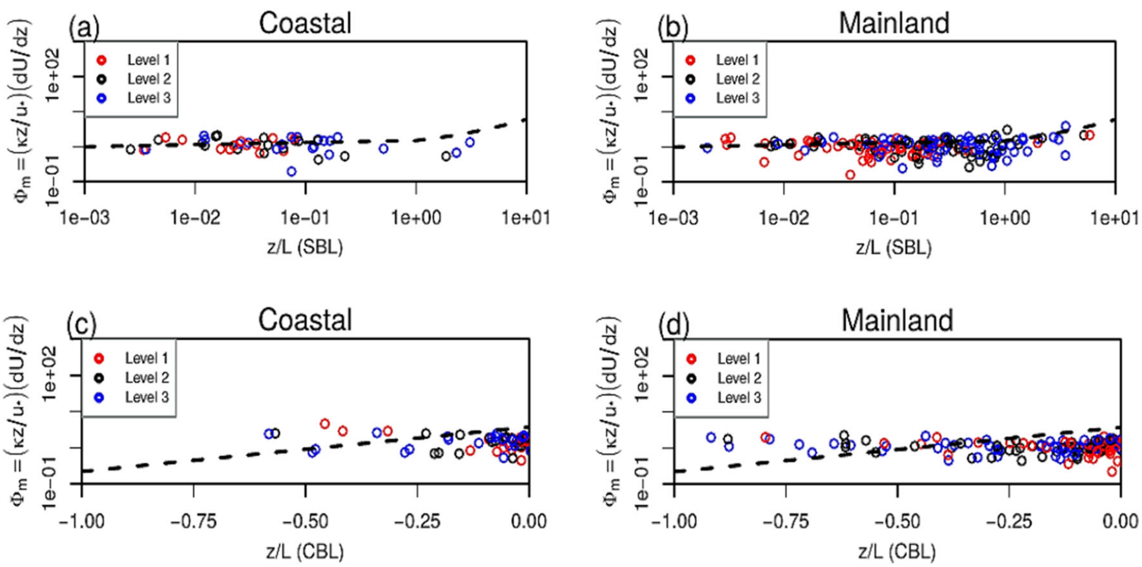

Figure 12. As for figure 9, but for the non-dimensional vertical gradient of mean wind speed (Φ_m). The dashed lines refer to the Businger–Dyer relationships $\Phi_m = (1 + 5\zeta)$ for $\zeta > 0$ **(a, b)** and $\Phi_m = (1 - 16\zeta)^{-1/4}$ for $\zeta < 0$ **(c, d)**.

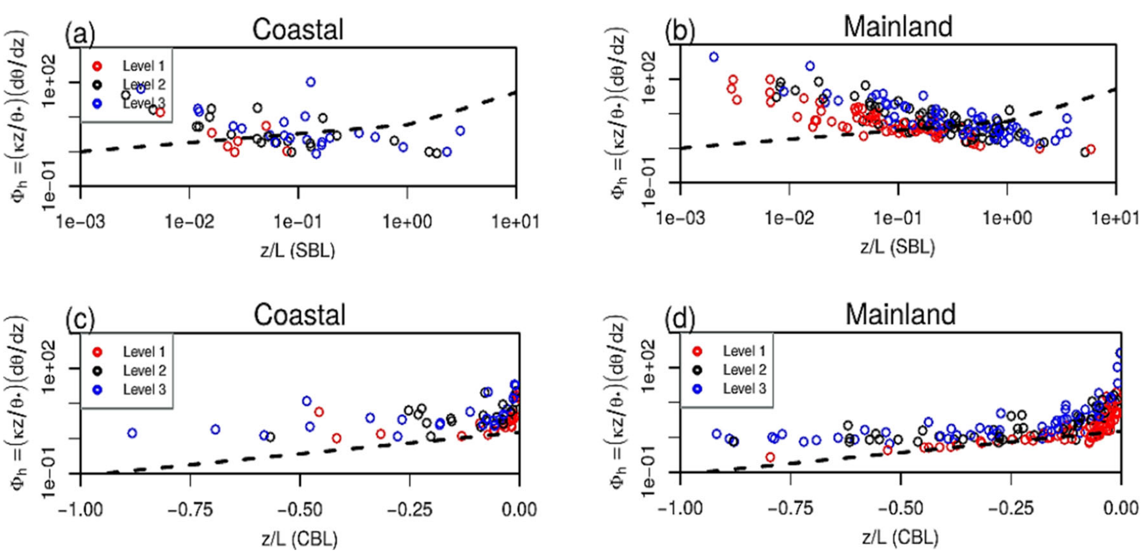

Figure 13. As for figure 9, but for the non-dimensional vertical gradient of mean potential temperature (Φ_h). The dashed lines refer to the Businger–Dyer relationships $\Phi_h = (1 + 5\zeta)$ for $\zeta > 0$ **(a, b)** and $\Phi_h = (1 - 16\zeta)^{-1/2}$ for $\zeta < 0$ **(c, d)**.

remaining systematically above it; this means that the variance of the non-dimensional vertical velocity is a universal function of ζ. It can, therefore, be assumed that Φ_w asymptotically follows the empirical Monin–Obukhov predictions, predicted for flat and homogeneous surfaces. The AMMA SOP3 data for Φ_w tend to overestimate the canonical Kansas-type expressions for $-1 < \zeta < 0$ (figure 15b, d). However, our Φ_w values better corroborate (for $0.01 < \zeta < 5$, figure 15c) the Kansas-type formulations under stable conditions while remaining slightly above them for several levels over the inland area; this can be explained by the fact that the stable stratification absorbs the vertical motion and the surface–turbulence interaction becomes nearly neutral. Similar results were achieved by Kaimal and Finnigan (1994) and Grachev *et al.* (2017), who proved that during onshore flow, the average data for Φ_w melt quite well and closely follow the canonical Monin–Obukhov predictions, valid for homogeneous and flat terrain, in the CASPER-East campaign. The bin-averaged Φ_w data for the coastal flow show less scatter between different collection levels (figure 15a) in a smaller range of the stability parameter ζ compared to the Φ_w values for the

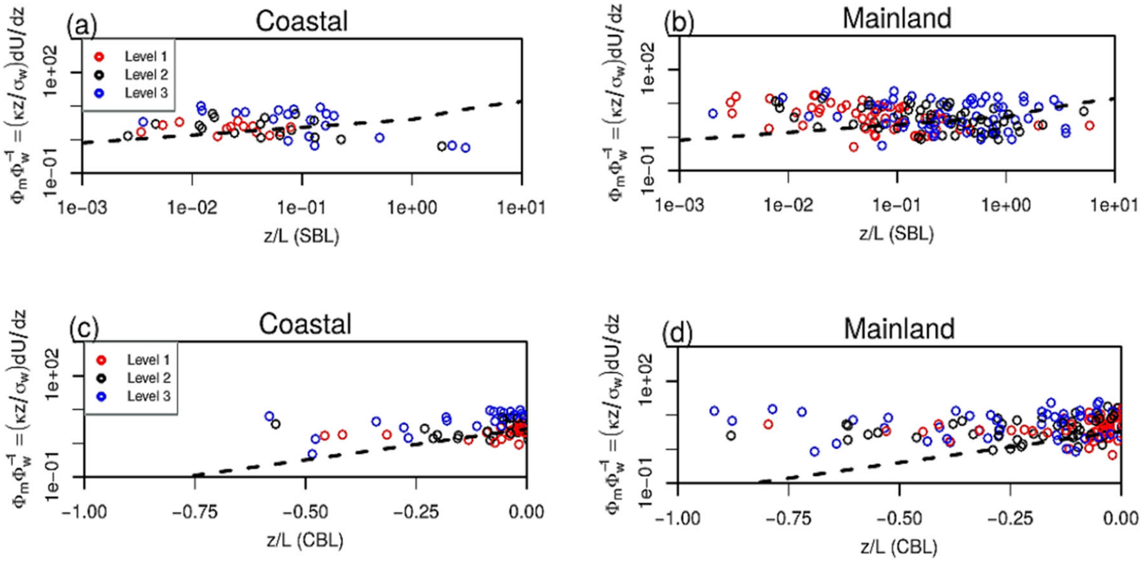

Figure 14. As for figure 9, but for the function $\Phi_m\Phi_w^{-1} = (\kappa z/\sigma_w)dU/dz$, which is a composite of the universal functions (5) and (6), for $\alpha = w$, and is not impacted by auto-correlation. The dashed lines refer to $\Phi_m\Phi_w^{-1} = 0.8(1+5\zeta)(1+0.2\zeta)^{-1}$ for $\zeta > 0$ **(a, b)** and $\Phi_m\Phi_w^{-1} = 0.8(1-16\zeta)^{-1/4}(1-3\zeta)^{-1/3}$ for $\zeta < 0$ **(c, d)**.

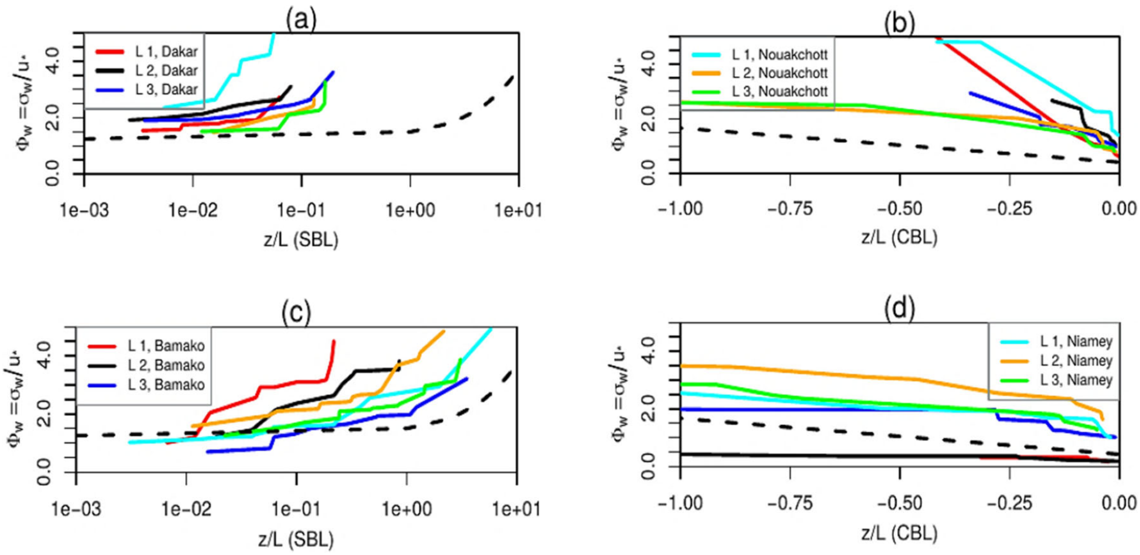

Figure 15. The bin-averaged non-dimensional universal functions of the vertical velocity component (Φ_w) plotted versus the local MOSP (ζ) for the nightly averages data recorded during the AMMA SOP3 field experiment (August 15–September 15, 2006) over two examples (Dakar and Nouakchott) of the coastal **(a, b)** and two examples (Bamako and Niamey) of the mainland **(c, d)** footprints. (a and c) correspond to stable conditions ($\zeta > 0$); (b and d) reflect the unstable conditions ($\zeta < 0$). The black dashed lines represent the Businger–Dyer relationships reported by Kaimal and Finnigan (1994).

inland flow (figure 15c) under stable conditions. The reason for this statement is that the ζ values are essentially closer around a mean value on the coast (too complex terrain), while the scatter is more pronounced in the mainland.

Figures 16 and 17 correspond to plots of bin-averaged mean wind speed Φ_m (figure 16) and mean temperature Φ_h (figure 17) as a function of ζ for our two surface types. A weak match emerges in these two figures with the canonical Monin–Obukhov Kansas-type predictions (plotted as dashed lines), contrasting with the Φ_w data. The bin-averaged Φ_m and Φ_h data obtained at different surface layer levels do not collapse entirely to a single curve, both in the coastal and inland areas, with a tendency for our observations to underestimate the MOST predictions. The dependence of Φ_m and Φ_h on ζ appears to be very weak. However, the existing gap between the bin-averaged values versus MOST expressions for Φ_m (figure 16) is less

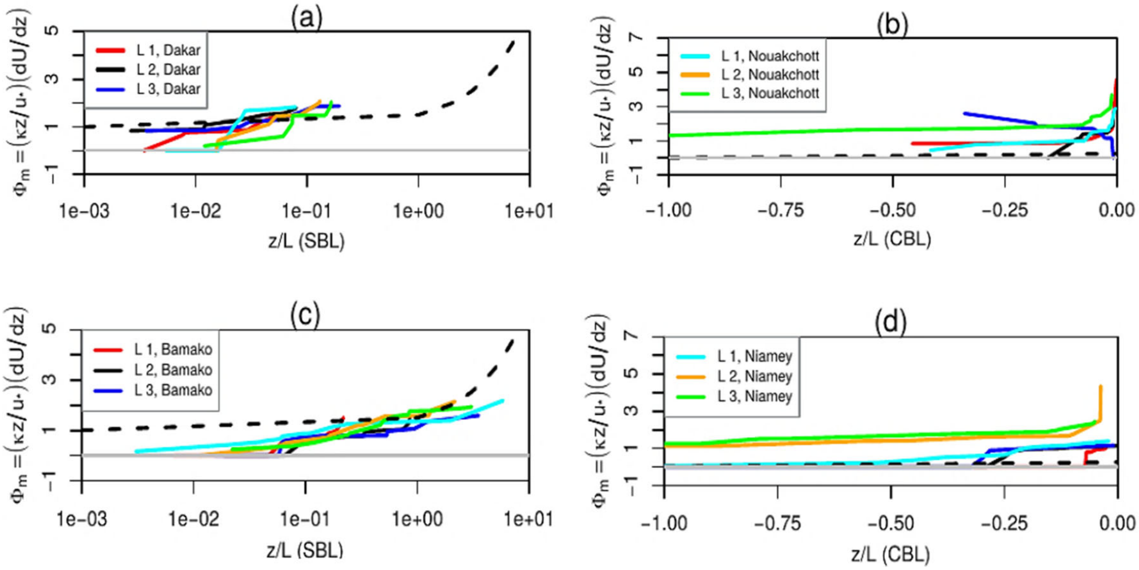

Figure 16. As for figure 15, but for the non-dimensional vertical gradient of mean wind speed (Φ_m). The dashed lines refer to the Kansas experiment type-relationships output by Kaimal and Finnigan (1994). The horizontal gray line corresponds to $\Phi_m = 0$.

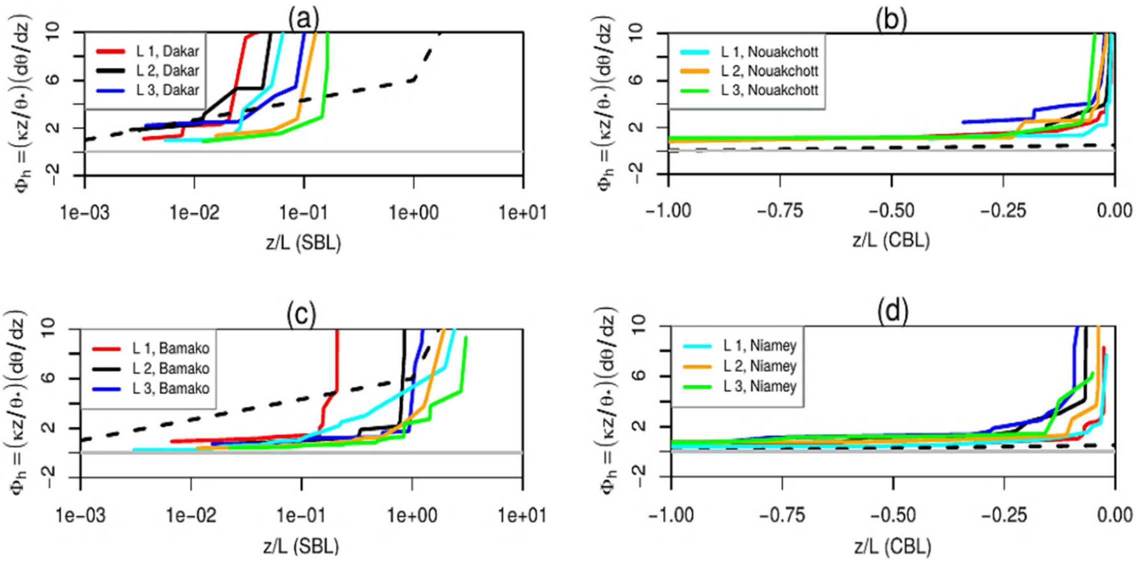

Figure 17. As for figure 15, but for the non-dimensional vertical gradient of mean potential temperature (Φ_h). The dashed lines correspond to the Kansas experiment type-relationships written by Kaimal and Finnigan (1994). The horizontal gray line corresponds to $\Phi_h = 0$.

pronounced than that for Φ_h. Thus, we can note that the curves for Φ_m versus ζ are qualitatively better behaved as they collapse relatively well with the classical functions than the curves for Φ_h.

The representations of our different universal functions follow various behaviours depending on the case. This diversification of behaviours can be attributed to the local (haze, sinuous motion, small eddies) and non-local (momentum and heat dynamics) turbulent effects at small scales in the ABL. At these scales, these effects adapt instantaneously to changes in local conditions (due to surface heterogeneity) at large scales, allowing to maintain a dynamic thermal equilibrium caused by the large eddies. The standard deviations obtained in this work were reasonably expected due to the fact that the MOST were established for local scale turbulence and non-neutral conditions and, thus, for inhomogeneous terrains such as those studied here. Similarly, the derivatives of the expressions for the vertical gradients of mean wind speed and potential temperature in Φ_m and Φ_h, whose estimates are based on a deep layer Δz, are mass parameters. Overall, large motions (e.g., due to irregular surface heat and pressure variations) as well as eddy dispersion control the mean vertical gradients. Large eddies enhanced by the surface texture are responsible for transporting heat and momentum throughout the depth of the ABL. Under these conditions, vertical and local gradients can have opposite directions. For this reason, classical MOST models are said to overlook the dynamics of non-local effects in the ABL.

The statement made in the above paragraph can be considered as a specific approach to the study of classical MOST. Indeed, the study of the generalized classical MOST implies the integration of additional influences on the flux-gradient relations, namely the boundary layer height, the thermal conductivity, the Coriolis parameter and several other statistics.

5. Conclusion

Using radiosonde data collected during the AMMA SOP3 field experiment conducted from August 15 to September 15, 2006 (summer monsoon) in West Africa, we examined local (small-scale) atmospheric turbulence data. These data were observed on three levels of the ABL surface layer over two types of terrain, including coastal and inland footprints. Based on the good resolution of these radiosonde data, we performed a spatio-temporal analysis of the ABL structure under non-stationary conditions to understand the coastal/inland air coupling. They enabled a comparative study of turbulent fluxes with other statistics over a range of aerodynamically rough and dry footprints, and relatively smooth and less dry footprints.

- A time-series analysis of the nightly averages of turbulent fluxes at each site was first performed. Unstable ($\zeta < 0$) and stable ($\zeta > 0$) stratifications were observed on each footprint type and site. Several time series of the different turbulent fluxes are similar from one surface to another. However, there are significant differences related to the thermal and aerodynamic properties of the lower surfaces. Although the differences between the drag coefficient, friction velocity as well as latent heat flux are not very noticeable, i.e., having the same order of magnitude for our range of surfaces, the nightly averages of the sensible heat flux are, however, more pronounced over the inland surfaces than over the coastal surfaces, due to the discontinuity of the heat capacity between the areas. Thus, sensible heat flux can be viewed as an indicator of different surface types.
- We basically focused on testing and approving MOST on the surface types using the dimensionless empirical functions according to MOST plotted as a function of ζ for the stable and unstable conditions, as well as the bin-averaged values scaled versus ζ. The scatter plots of the nightly averages of the individual values of the scaled classical functions of Φ_w, Φ_u, and Φ_θ prove that the dimensionless standard deviations globally adhere to MOST within the stability conditions and the uncertainty of the experiment. Furthermore, the scatter of the Φ_θ data compared to the classical MOST curves is likely to be related to heterogeneous field temperature. Also, statistically, Φ_w has a better MOSP dependence than Φ_u. A careful study of the bin-averaged plotted data shows that Φ_w converges better at multi-level to a single universal Kansas-type curve for inland flow than for coastal flow while remaining consistently above it in the ranges $0.01 < \zeta < 5$ and $-1 < \zeta < 0$.
- The dimensionless vertical gradient of mean wind speed Φ_m and potential temperature Φ_θ for our observations on the coast show a poor match with the Businger–Dyer and Monin–Obukhov empirical predictions than inland. Compared to Φ_w, Φ_h and Φ_m show, statistically, very little or no dependence on ζ. This suggests that coastal flow requires coastal-specific coding.
- In view of the above, we can say that the conjunction of local and non-local turbulent effects is responsible for the divergent behaviour of the diverse universal functions in the ABL. The turbulent measurements observed at a single level enabled us to establish the scaled deviations of MOST associated with uncodified small- and large-scale turbulent motions (small and large eddies, for example). However, local features of the airflow (local small-scale fluxes and gradients) are strongly responsible for small-scale turbulence, while large-scale forcing has less influence on stratification. Since the flux–profile relationships are based on measurements inside the thick layers and controlled by motions and structures (small eddies, small structures, and other local motions) considered as 'noises', the classical expressions become inadequate to describe Φ_h and Φ_m in the coastal environment. Thus, the coastal zone, which is the sea/land interface, becomes more complex and deserves

further investigations to obtain a better match of Φ_h and Φ_m with the classical MOST functions.

Acknowledgements

The authors would like to thank the AMMA database community for the radiosonde data. The authors gratefully acknowledge the anonymous reviewers and the associate editor for their constructive comments and valuable suggestions, which significantly improved the presentation of the final manuscript.

Author statement

Gislain R Mekompoamb: Conceptualization, methodology, data curation, numerical modelling, formal analysis, writing – original draft. André Lenouo: Conceptualization, data curation, writing – review and editing of the draft manuscript. Clément Tchawoua: Visualization, supervision.

References

Agusti P A, Beljaars A, Ahlgrimm M, Balsamo G, Bock O, Forbes R, Ghelli A, Guichard F, Köhler M, Meynadier R and Morcrette J J 2010 The ECMWF re-analysis for the AMMA observational campaign; *Q. J. R. Meteorol. Soc.* **136** 1457–1472, https://doi.org/10.1002/qj.662.

Baklanov A A, Grisogono B, Bornstein R, Mahrt L, Zilitinkevich S S, Taylor P, Larsen S E, Rotach M W and Fernando H J S 2011 The nature, theory, and modeling of atmospheric planetary boundary layers; *Bull. Am. Meteor. Soc.* **92** 123–128, https://doi.org/10.1175/2010BAMS2797.1.

Bech J, Bebbington D H, Codina B, Sairouni A and Lorente J 1998 Evaluation of atmospheric anomalous propagation conditions: An application for weather radars; In: Remote sensing for agriculture, ecosystems, and hydrology (ed.) Engman E T, *Inter. Soc. Optical Eng.* **3499** 111–113.

Brooks I M, Goroch A K and Rogers D P 1999 Observations of strong surface radar ducts over the Persian Gulf; *J. Appl. Meteor.* **38**(**9**) 1293–1310, https://doi.org/10.1175/1520-0450(1999)038%3c1293:OOSSRD%3e2.0.CO;2.

Businger J A, Wyngaard J C, Izumi Y and Bradley E F 1971 Flux–profile relationships in the atmospheric surface layer; *J. Atmos. Sci.* **28** 181–189, https://doi.org/10.1175/1520-0469(1971)028%3c0181:FPRITA%3e2.0.CO;2.

Deardorff J W 1972 Numerical investigation of neutral and unstable planetary boundary layers; *J. Atmos. Sci.* **29** 91–115, https://doi.org/10.1175/1520-0469(1972)029%3c0091:NIONAU%3e2.0.CO;2.

Faccani C, Rabier F, Fourrié N, Agusti-Panareda A, Karbou F, Moll P, Lafore J-P, Nuret M, Hdidou F and Bock O 2009 The impacts of AMMA radiosonde data on the French global assimilation and forecast system; *Wea. Forecasting* **24** 1268–1286, https://doi.org/10.1175/2009WAF2222237.1.

Flamant C, Knippertz P, Fink A H, Akpo A, Brooks B, Chiu H, Coe H, Danuor S, Evans M, Jegede O, Kalthoff N, Konaré A, Liousse C, Lohou F, Mari C, Schlager H, Schwarzenboeck A, Adler B, Amekudzi L, Aryee J, Ayoola M, Batenburg M, Bessardon G, Borrmann S, Brito J, Bower K, Burnet F, Catoire V, Colomb A, Denjean C, Fosu-Amankwah K, Hill P, Lee J, Lothon M, Maranan M, Marsham J, Meynadier R, Ngamini J, Rosenberg P, Sauer D, Smith V, Stratmann G, Taylor C, Voigt C and Yoboué V 2017 The dynamics–aerosol–chemistry–cloud interactions in West Africa field campaign: Overview and research highlights; *Bull. Am. Meteor. Soc.*, https://doi.org/10.1175/BAMS-D-16-0256.1.

Garratt J R 1992 *The atmospheric boundary layer*; Cambridge University Press, Cambridge.

Geernaert G L 1988 Drag coefficient modelling for the near-coastal zone; *Dyn. Atmos. Oceans* **11**(**3–4**) 307–322, https://doi.org/10.1016/0377-0265(88)90004-8.

Glazunov A, Rannik Ü, Stepanenko V, Lykosov V, Auvinen M, Vesala T and Mammarella I 2016 Large-eddy simulation and stochastic modeling of Lagrangian particles for footprint determination in the stable boundary layer; *Geos. Model Dev.* **9** 2925–2949, https://doi.org/10.5194/gmd-9-2925-2016.

Goutorbe J-P, Lebel T, Tinga A, Bessemoulin P, Brouwer J, Dolman A J, Engman E T, Gash J H C, Hoepffner M, Kabat P, Kerr Y H, Monteny B, Prince S, Said F, Sellers P and Wallace J S 1994 HAPEX-Sahel: A large-scale study of land–atmosphere interactions in the semi-arid tropics; *Ann. Geophys.* **12** 53–64.

Grachev A A, Boulder C O, Fairall C W, Persson P O G, Andreas E L, Guest P S and Jordan R E 2003 Turbulence decay in the stable Arctic boundary layer; *Seventh Conference on Polar Meteorology and Oceanography and Joint Symposium on High-Latitude Climate Variations.*

Grachev A A, Fairall C W, Persson P O G, Andreas E L and Guest P S 2005 Stable boundary-layer scaling regimes: The SHEBA data; *Bound.-Layer Meteorol.* **116**(**2**) 201–235, https://doi.org/10.1007/s10546-004-2729-0.

Grachev A A, Andreas E L, Fairall C W, Guest P S and Persson P O G 2008 Turbulence measurements in the stable atmospheric boundary layer during SHEBA: Ten years after; *Acta Geophys.* **56**(**1**) 142–166, https://doi.org/10.2478/s11600-007-0048-9.

Grachev A A, Leo L S, Di Sabatino S, Fernando H J S, Pardyjak E R and Fairall C W 2016 Structure of turbulence in katabatic flows below and above the wind-speed maximum; *Bound.-Layer Meteorol.* **159** 469–494, https://doi.org/10.1007/s10546-015-0034-8.

Grachev A A, Leo L S, Fernando J S H, Fairall C W, Creegan E, Blomquist B W, Christman A J and Hocut C M 2017 Air–sea/land interaction in the coastal zone; *Bound.-Layer Meteorol.* **167**(**2**) 181–210, https://doi.org/10.1007/s10546-017-0326-2.

Guichard F, Asencio N, Peugeot C, Bock O, Redelsperger J L, Cui X, Garvert M, Lamptey B, Orlandi E, Sander J, Fierli F, Gaertner M A, Jones S, Lafore J P, Morse A, Nuret M, Boone A, Balsamo G, De Rosnay P, Decharme B, Harris P P and Berges J C 2010 An intercomparison of simulated rainfall and evapotranspiration associated with a mesoscale convective system over West Africa; *Wea. Forecasting* **25** 37–60, https://doi.org/10.1175/2009WAF2222250.1.

Högström U 1988 Non-dimensional wind and temperature profiles in the atmospheric surface layer: A re-evaluation; *Bound.-Layer Meteorol.* **42(1)** 55–78, https://doi.org/10.1007/BF00119875.

Holtslag A A M, Svensson G, Baas P, Basu S, Beare B, Beljaars A C M, Bosveld F C, Cuxart J, Lindvall J, Steeneveld G J *et al.* 2013 Stable atmospheric boundary layers and diurnal cycles: Challenges for weather and climate models; *Bull. Am. Meteorol. Soc.* **94** 1691–1706, https://doi.org/10.1175/BAMS-D-11-00187.1.

Kaimal J C and Finnigan J J 1994 *Atmospheric boundary layer flows: Their structure and measurements*; Oxford University Press, Oxford.

Kaissassou S, Lenouo A, Tchawoua C, Lopez P and Amadou T 2015 Climatology of anomalous propagation radar over West Africa; *J. Atmos. Sol.-Terr. Phys.* **123** 1–12, https://doi.org/10.1016/j.jastp.2014.11.009.

Kaissassou S, Lenouo A, Tanessong R S, Tamo K, Vondou A, Pokam W and Kanko J 2020 Investigation of anomalous propagation conditions in Central and West Africa stations using high-resolution GPS radiosonde observations; *J. Earth Syst. Sci.* **129** 220, https://doi.org/10.1007/s12040-020-01477-y.

Kaissassou S, Djiotang L, Komkoua A, Ekobo B, Ndzana B, Tanessong R, Guenang M and Vondou A 2021 Climatology of super-refraction and trapping layers conditions over Central and West Africa; *Meteor. Appl.* **28(4)** e2016, https://doi.org/10.1002/met.2016.

Karbou F, Beucher F, Bock O, Lafore J P, Mumba Z, Ngamini J B, Nuret M, Rabier F and Redelsperger J L 2012 Les leçons de l'expérience AMMA en matière de prévision numérique du temps; *La Météorologie-Spécial AMMA* 49–54, https://doi.org/10.4267/2042/48132.

Klaassen W and Sogachev A 2006 Flux footprint simulation downwind of a forest edge; *Bound.-Layer Meteorol.* **121(3)** 459–473, https://doi.org/10.1007/s10546-006-9078-0.

Kljun N, Calanca P, Rotach M W and Schmid H P 2004 A simple parameterization for flux footprint predictions; *Bound.-Layer Meteorol.* **112(3)** 503–523, https://doi.org/10.1023/B:BOUN.0000030653.71031.96.

Leclerc M Y and Foken T 2014 *Footprints in micrometeorology and ecology*; Springer, Berlin, https://doi.org/10.1007/978-3-642-54545-0.

Mahrt L and Geernaert G L 1999 *Air–sea exchange: Physics chemistry and dynamics*; Kluwer Academic Publishers, Dordrecht, pp. 247–268.

Mahrt L, Sun J, Blumen W, Delany T and Oncley S 1998 Nocturnal boundary-layer regimes; *Bound-Layer Meteorol.* **88** 255–278, https://doi.org/10.1023/A:1001171313493.

Mentes S and Kaymaz Z 2007 Investigation of surface duct conditions over Istanbul, Turkey; *J. Appl. Meteor. Clim.* **46** 318–337, https://doi.org/10.1175/JAM2452.1.

Merry M and Panofsky H A 1976 Statistics of vertical motion over land and water; *Quart. J. Roy. Meteor. Soc.* **102** 255–260, https://doi.org/10.1002/qj.49710243120.

Mesnard F and Sauvageot H 2010 Climatology of anomalous propagation radar echoes in a coastal area; *J. Appl. Meteor. Climatol.* **49** 2285–2300, https://doi.org/10.1175/2010JAMC2440.1.

Moeng C-H and Sullivan P P 1994 A comparison of shear- and buoyancy-driven planetary boundary layer flows; *J. Atmos. Sci.* **51** 999–1022, https://doi.org/10.1175/1520-0469(1994)051%3c0999:ACOSAB%3e2.0.CO;2.

Monin A S and Obukhov A M 1954 Basic laws of turbulent mixing in the surface layer of the atmosphere; *Trudy Geofiz Inst Acad Nauk SSSR* **24(151)** 163–187.

Nadeau D F, Pardyjak E R, Higgins C W and Parlange M B 2013 Similarity scaling over a steep alpine slope; *Bound.-Layer Meteorol.* **147(3)** 401–419, https://doi.org/10.1007/s10546-012-9787-5.

Nieuwstadt F T M 1984 The turbulent structure of the stable, nocturnal boundary layer; *J. Atmos. Sci.* **41** 2202–2216, https://doi.org/10.1023/A:1001158702252.

Panofsky H A and Dutton J A 1984 *Atmospheric turbulence: Models and methods for engineering applications*; Wiley, New York.

Penide G, Giraud V, Bouniol D, Dubuisson P, Duroure C, Protat A and Cautenet S 2010 Numerical simulation of the 7 to 9 September 2006 AMMA mesoscale convective system: Evaluation of the dynamics and cloud microphysics using synthetic observations; *Quat. J. Roy. Meteor. Soc.* **136(s1)** 304–322, https://doi.org/10.1002/qj.558.

Rannik Ü 1998 On the surface layer similarity at a complex forest site; *J. Geophys. Res.* **103(D8)** 8685–8697, https://doi.org/10.1029/98JD00086.

Redelsperger J L, Thorncroft C D, Diedhiou A, Lebel T, Parker D J and Polcher J 2006 African monsoon multidisciplinary analysis, an international research project and field campaign; *BAMS* **87** 1736–1746.

Sorbjan Z 1989 *Structure of the atmospheric boundary layer*; Prentice-Hall, Englewood Cliffs.

Steinbrecht W, Claude H, Schönenborn F, Leiterer U, Dier H and Lanzinger E 2008 Pressure and temperature differences between Vaisala RS80 and RS92 radiosonde systems; *J. Atmos. Ocean Technol.* **25(6)** 909–927, https://doi.org/10.1175/2007jtecha999.1.

Steiner M and Smith J A 2002 Use of three-dimensional reflectivity structures for automated detection and removal of non-precipitating echo in radar data; *J. Atmos. Ocean Technol.* **19** 673–686, https://doi.org/10.1175/1520-0426(2002)019%3c0673:UOTDRS%3e2.0.CO;2.

Stull R B 1988 *An introduction to boundary-layer meteorology*; Kluwer Academic Publishers, Boston.

Wyngaard J C 2010 *Turbulence in the atmosphere*; Cambridge University Press, New York.

Corresponding editor: Parthasarathi Mukhopadhyay